Hilltop Curvature Increases with the Square Root of Erosion Rate

Hilltop Curvature Increases with the Square Root of Erosion Rate

E. J. Gabet[1], S. M. Mudd[2], R. W. Wood[1], S. W. D. Grieve[3], S. A. Binnie[4], T. J. Dunai[4]

[1] Department of Geology, San Jose State University, San Jose, California, 95192, USA.
[2] School of Geosciences, University of Edinburgh, Edinburgh, UK, EH9 3FE.
[3] School of Geography, Queen Mary University of London, London, UK, E1 4NS.
[4] Institute for Geology and Mineralogy, University of Cologne, Germany, 50674.

Corresponding author: Emmanuel Gabet (manny.gabet@sjsu.edu)

Key Points:

- Hilltop curvature at our sites does not vary linearly with erosion rate, as predicted by theory
- The inferred transport coefficient appears to be insensitive to climate
- Processes affecting the underlying bedrock may control the shape of soil-mantled hillslopes

Abstract

The shape of soil-mantled hillslopes is typically attributed to erosion rate and the transport efficiency of the various processes that contribute to soil creep. While climate is generally hypothesized to have an important influence on soil creep rates, a lack of uniformity in the measurement of transport efficiency has been an obstacle to evaluating the controls on this important landscape parameter. We addressed this problem by compiling a data set in which the transport efficiency has been calculated using a single method, the analysis of hilltop curvatures using 1-m LiDAR data, and the erosion rates have also been determined via a single method, *in-situ* cosmogenic ^{10}Be concentrations. Moreover, to control for lithology, we chose sites that are only underlain by resistant bedrock. The sites span a range of erosion rates (6 – 922 mm/kyr), mean annual precipitation (39 – 320 cm/yr), and aridity index (0.08 – 1.38). Surprisingly, we find that hilltop curvature varies with the square root of erosion rate,

whereas previous studies predict a linear relationship. In addition, we find that the inferred transport coefficient also varies with the square root of erosion rate but is insensitive to climate. We explore various mechanisms that might link the transport coefficient to the erosion rate and conclude that present theory regarding soil-mantled hillslopes is unable to explain our results and is, therefore, incomplete. Finally, we tentatively suggest that processes occurding in the bedrock (e.g., fracture generation) may play a role in the shape of hillslope profiles at our sites.

Index Terms: 1826, 1819, 1862

1. Introduction

On soil-mantled surfaces too gentle for significant landsliding, particles are primarily transported downslope by soil creep. Soil creep is a general term for the cumulative effect of myriad individual processes that locally disturb soil, such as the freezing and thawing of pore water [*Anderson et al.*, 2013], shrink-swell cycles [*Carson and Kirkby*, 1972], dry ravel [*Anderson et al.*, 1959; *Gabet*, 2003], burrowing by animals [*Gabet et al.*, 2003], and tree throw [e.g., *Denny and Goodlett*, 1956]. Culling [1963] proposed that the rate of soil creep (q_s; L^2/T) is linearly proportional to hillslope gradient, S (L/L), such that

$$q_s = DS \tag{1}$$

where D (L^2/T) is a sediment transport coefficient. The sediment transport coefficient, D, is a measure of the efficiency of the various soil creep processes, and its magnitude sets the pace for hillslope evolution [e.g., *Fernandes and Dietrich*, 1997; *Roering et al.*, 1999]. Although a nonlinear relationship between gradient and flux is supported by topographic analysis [*Andrews and Bucknam*, 1987; *Grieve et al.*, 2016; *Hurst et al.*, 2012; *Roering et al.*, 1999]

53 and physical simulations [*Gabet*, 2003; *Roering et al.*, 2001b], this relationship reduces to
54 Eqn. (1) on slopes < 20° [*Hurst et al.*, 2012].

55 Our understanding of the controls on *D* for a particular landscape is limited. Because
56 soil creep processes are typically climatically controlled, either directly (e.g., freeze-thaw) or
57 indirectly through climate's effect on the distribution of the biota, temperature and
58 precipitation are expected to have a dominant role in the transport efficiency of soil creep
59 [e.g., *Dunne et al.*, 2010; *Hanks*, 2000; *Pelletier et al.*, 2011]. Indeed, Hurst et al. [2013] and
60 Richardson et al. [2019] found that *D* increases with mean annual precipitation, albeit
61 weakly; the latter also found that *D* increases with the aridity index, which is the ratio
62 between precipitation and evapotranspiration [*Trabucco and Zomer*, 2019]. In contrast, Ben-
63 Asher et al. [2017] concluded that transport efficiency decreases with precipitation, although
64 this result was based on a small data set. Soil thickness [*Furbish et al.*, 2009; *Heimsath et al.*,
65 2005] and soil texture [*Furbish et al.*, 2009], as well as underlying lithology [*Hurst et al.*,
66 2013], may also be important factors. A lack of uniformity in measuring *D*, however, has
67 been an obstacle in investigating the effect of these various factors.

68 Determining the controls on the transport coefficient is important for a variety of
69 reasons. Because many landscapes are soil-mantled, not affected by overland flow, and too
70 gentle for significant landsliding, Eqn. (1) and its nonlinear counterpart are thought to offer a
71 complete description (or nearly so) of sediment transport across much of the Earth's surface.
72 Moreover, assuming steady-state topography, combining Eqn. (1) with a statement of mass
73 conservation yields

74 $$C_{HT} = -\frac{E}{D}\left(\frac{\rho_s}{\rho_r}\right) \qquad (2)$$

where E is the erosion rate (L/T), C_{HT} (1/L) is the two-dimensional curvature (i.e., the Laplacian of elevation) of a hill's ridgecrest, and ρ_s and ρ_r are the density (L^3/T) of soil and rock, respectively [*Roering et al.*, 2007]. With this equation (and its nonlinear version), D and E are both assumed to be independent variables: E is controlled by the rate at which the lower boundary is lowered (e.g., via river incision in response to uplift), and D is controlled by the intensity of the various soil creep processes. According to this theory, the profile of a hillslope adjusts itself such that its curvature satisfies Eqn. (2) [*Culling*, 1963; *Gilbert*, 1909]. Therefore, understanding the controls on the transport efficiency should provide insight into hillslope form. In addition, studies have used Eqn. (1) and its nonlinear version to model the degradation of fault scarps to estimate earthquake recurrence interval [e.g., *Hanks and Schwartz*, 1987], and the results are sensitive to the value of the transport coefficient. Finally, understanding the role of the various factors on D is important as geologists attempt to infer erosion rates based on topographic analyses [*Hurst et al.*, 2012].

2. Methods

2.1. Site selection and descriptions

Appropriate sites were limited to watersheds which had both LiDAR and cosmogenic ^{10}Be data sets. The ^{10}Be data came from a global compilation [*Harel et al.*, 2016], and the associated LiDAR data were acquired from the OpenTopography (http://opentopo.sdsc.edu) and USGS (https://viewer.nationalmap.gov) platforms. LiDAR data with spatial resolutions coarser than 1-m cannot accurately resolve ridgeline curvatures in all settings [*Grieve et al.*, 2016] and so any sites without 1-m resolution data were excluded from the analysis. Because ridgeline curvatures were used to estimate D (see below), only watersheds that appeared to be in topographic steady-state were chosen. For example, watersheds with clear knickpoints

or with asymmetrical ridges were avoided, as well as steep watersheds advancing into low-relief surfaces. Simulations of hillslope evolution suggest that hillslopes with declining erosion rates adjust so quickly that they are difficult to differentiate from steady state hillslopes; furthermore, hillslopes experiencing accelerated uplift only preserve the signature of changing erosion rates for tens of thousands of years [*Mudd*, 2017]. Therefore, by avoiding areas with obvious signs of landscape transience, we are less likely to find ridgeline curvatures reflective of transient conditions. Thirty sites from six regions in the United States met our criteria: the Olympic Peninsula (WA) [*Belmont et al.*, 2007], the Feather River area (CA) [*Hurst et al.*, 2012; *Riebe et al.*, 2001; *Saucedo and Wagner*, 1992], the San Gabriel Mountains (CA) [*DiBiase et al.*, 2010], Yucaipa Ridge (CA) [*Binnie et al.*, 2007], the Idaho Plateau (ID) [*Wood*, 2013], and the Blue Ridge Mountains (VA) [*Duxbury*, 2009] (Figure 1) . Some of the regions (e.g., the San Gabriel Mountains) had ^{10}Be data for sites not covered by available LiDAR data and, thus, their full data-sets could not be used. Climatic data for these sites were obtained from the 800-m resolution PRISM model [*PRISM*, 2014], which provides recent (1981 – 2010) 30-yr means for annual precipitation (MAP) and annual temperature (MAT) (Table 1). The aridity index for the sites was determined from Trabuco and Zomer [2019]. While these data are for the modern climate, we assume that they are representative (at least in a relative sense) of the climate state over the time-scale of the erosion rates measured with ^{10}Be (i.e., 10^3 - 10^5 yrs). To control for rock strength, we chose sites underlain by lithologies known to be resistant to erosion: plutonic and metamorphic bedrock [e.g., *Gabet*, 2020; *Hack*, 1973] (Table 1).

119 2.2. Erosion rate calculations

120 To ensure a consistent method for calculating erosion rates, they were determined
121 from ^{10}Be concentrations in detrital quartz grains (Table 1). For five of the study regions,
122 published ^{10}Be concentrations were used to calculate basin-scale erosion rates. For the Idaho
123 Plateau sites, ^{10}Be concentrations were measured from soil and fluvial sediment samples
124 collected for this study (see below). For all six study regions, erosion rates were calculated
125 from the ^{10}Be concentrations using a single algorithm [*Mudd et al.*, 2016].

126 A full description of the Idaho Plateau field area can be found in Wood [2013].
127 Ridgetop and basin-scale denudation rates were determined by measuring cosmogenic ^{10}Be
128 concentrations in quartz [*Brown et al.*, 1995; *Granger et al.*, 1996]. The ridgetop rates were
129 determined from soil samples taken from the top 20 cm of the regolith at three sites. For the
130 basin-scale erosion rates, fluvial sediment was taken from three 1st-order streams. Pure quartz
131 fractions from the crushed and sieved (250-710 µm) and magnetically separated samples
132 were obtained using published procedures [*Kohl and Nishiizumi*, 1992; *Mifsud et al.*, 2013].
133 ICP-OES analysis of purity was undertaken on splits of the etched quartz. Samples were
134 spiked with ~200 µg of a commercial Be carrier (Scharlab Berylium ICP standard solution)
135 and prepared as AMS targets at the University of Cologne using a standard sample
136 preparation method [2015]. The samples were prepared alongside a reagent blank; ^{10}Be
137 concentrations following blank subtraction are reported in Table 2. Blank corrections are <2
138 %, except for sample S2, for which the correction is <5 %. Samples were measured on
139 CologneAMS [*Dewald et al.*, 2013] and normalized to reference standards [2007].
140 Uncertainties in the concentrations are estimated by propagating the uncertainties of the

AMS measurements and mass of Be added during spiking (estimated 1σ uncertainty of 1%) of both the samples and the blank.

^{10}Be concentrations were converted to denudation rates with the CAIRN software package, which accounts for topographic shielding and snow shielding [*Mudd et al.*, 2016]. We calculated snow shielding by first fitting a bilinear trend in snow water equivalent (SWE) as a function of elevation based on regional climate data from the National Oceanic and Atmospheric Association [*NOAA*, 2016] and following Kirchner et al. [2014]. SWE averages were converted to snow shielding values by assuming that snow reduces production solely by spallation [*Mudd et al.*, 2016]. Snow shielding is highly uncertain because of the difficulty of estimating the average SWE over the timescales of 10^3 – 10^4 years. We calculated denudation rates with no snow shielding to assess the sensitivity of denudation rate to snow thickness and found that, without accounting for snow, denudation rate estimates could be as much as 15% higher (for sample S3) but, for most samples, the differences were less than 10%. Uncertainties from analytical error and from uncertainties in production scaling and shielding are presented in Table 1 [*Mudd et al.*, 2016].

2.3. Transport Coefficient Calculations

Direct estimates of the transport efficiency by field measurements of sediment fluxes over the relevant time and spatial scales across a range of landscapes are impractical. Instead, along ridgelines, where slopes are gentle and soil creep is well described by Eqn. (1), the transport coefficient can be calculated by rewriting Eqn. (2) as

$$D = -\left(\frac{E}{C_{HT}}\right)\left(\frac{\rho_r}{\rho_s}\right) \quad (3).$$

The ratio ρ_r/ρ_s was assumed to be 2 [*Hurst et al.*, 2012]; this value is probably only approximately correct for each of our sites and likely varies by ±25%. Ridgeline curvatures were calculated from a 1-m LiDAR DEM for each site using a six-term polynomial function to fit the elevation data within a circular sliding window with a diameter of 14 m. A value of 14 m for the analysis window was chosen based on sensitivity analyses presented in Grieve et al. [2016] which followed the method for identifying the optimal window diameter described in Roering et al. [2010] and Hurst et al. [2012].

The second derivative of the polynomial function at the window's center is that cell's two-dimensional curvature. Because topographic noise could produce outliers, the median of the curvatures along each watershed's ridgeline was used in our analyses [*Hurst et al.*, 2012]. The average slopes (± 1σ) along the ridgelines, determined as the first derivative of the polynomial function, ranged from 0.5 ± 3° (Blue Ridge Mtns) to 9 ± 6° (Yucaipa Ridge), thereby validating the use of Eqn. (1). Note that, even at the steepest site along Yucaipa Ridge, nearly 95% of the area analyzed had slopes < 20°. Finally, an automated procedure was used to detect the presence of bedrock outcrops along the ridgelines [*Milodowski et al.*, 2015] to confirm that the sites were mantled with soil. One Yucaipa Ridge site had 75% soil-cover and the other had 90% soil-cover; the soil-cover at the other sites ranged from 97 to 100%. Observations of Google Earth™ imagery supported these estimates.

2.3 Additional Data

The dataset described above was supplemented with data selected from a compilation presented in Richardson et al. [2019] (Table 1). From this compilation, four sites met our criteria: the ridgelines were symmetrical, transport coefficients were estimated by analyzing ridgetop curvatures from 1-m LiDAR data, erosion rates were determined with cosmogenic

^{10}Be, and the soils were derived from resistant lithologies (Table 1). The only difference is that Richardson et al. used a 15-m window for their curvature analysis whereas our study used a 14-m window; we consider this difference to be insignificant. With the combined datasets, the sites represent a range of erosion rates from 6 to 922 mm/kyr, a range of mean annual precipitation from 39 to 320 cm/yr, a range of mean annual temperature from 2 to 15° C, and range of aridity index from 0.08 to 1.38 (Table 1).

2.4 Correcting for Grid Resolution

As erosion rates increase, ridgelines become sharper, which could potentially weaken the ability to accurately measure curvature given a fixed grid resolution. In particular, this grid-resolution effect could lead to an increasing underestimate of curvature as ridgelines sharpen with increasing erosion rates, thereby artificially introducing a positive relationship between *D* and *E*. To correct for this potential artefact, we performed an analysis in which we compared the estimates of the transport efficiency with those from idealized one-dimensional (1D) hillslopes. We assumed our ridges can be approximated as one-dimensional because curvature perpendicular to ridgelines far exceeds curvature parallel to our ridgelines.

To begin, we solved for the elevation of an idealized 1D hillslope by assuming that a nonlinear sediment flux law describes sediment transport on our hillslopes [e.g., *Andrews and Bucknam*, 1987; *Roering et al.*, 1999]

$$q_s = -\frac{D\frac{\partial z}{\partial x}}{1-\left(\left|\frac{\partial z}{\partial x}\right| \Big/ S_c\right)^2} \qquad (4)$$

where q_s is sediment flux (m^2/yr), D is the sediment transport coefficient (m^2/yr), z is the surface elevation, x is a horizontal distance, and S_c is a critical slope angle. As noted earlier,

this equation reduces to Eqn. (1) at gentle slopes. Inserting Eqn. (4) into a statement of mass conservation and solving it under steady-state conditions yields an expression for the elevation of a hillslope [*Roering et al.*, 2001a]:

$$z = -\frac{S_c^2}{2\beta}\left[\sqrt{D^2 + \left(\frac{2\beta x}{S_c^2}\right)} - D\ln\left(\frac{S_2}{2\beta}\sqrt{D^2 + \left(\frac{2\beta x}{S_c^2}\right)^2} + \frac{S_c D}{2\beta}\right)\right] + c \quad (5)$$

where β is the ratio between rock and soil density multiplied by the erosion rate ($(\rho_r/\rho_s)*E$) and c is a constant that sets the absolute elevation of the hillslope profile. At the divide (x = 0 m), the curvature is equal to:

$$\left(\frac{d^2 z}{dx^2}\right)_{HT} = -\frac{\beta}{D} \quad (6).$$

As described earlier, curvature at each site was measured from gridded 1-m topographic data. To mimic this procedure on the synthetic hillslope, we solved Eqn. (5) on a grid of points with a spacing of 1 m. Random noise was then imposed on each gridded data point from a uniform distribution ranging from -0.1 to 0.1 m, which is a conservative estimate of vertical error in typical airborne LiDAR data. As with the real landscapes, a 2nd-order polynomial equation was fitted across the ridgetop over a 14-m window and the curvature was calculated at the center node.

However, in any gridded topography, the highest true elevation of the ridge may not be located exactly on the grid sampling point. The exact location of the ridge may be offset from the highest gridded pixel by up to half a pixel width. In Eqn. (5), the ridge is located at x = 0 meters, but to account for the possibility that the ridgeline does not correspond to the highest pixel, we allowed the gridded points to shift laterally by 0.5 m to produce an offset between the center point in the gridded data and the ridgeline.

227 For each study site (Table 1), the values of β and S_c were calculated using the erosion
228 rate and measured curvature to produce idealized ridgetop profiles. Random noise was then
229 applied to the profile, the grid was shifted, and the 'synthetic' curvature was calculated from
230 the fitted 2nd-order polynomial. This process was repeated with variations in D until the
231 synthetic curvature matched the curvature measured from the topographic data. We
232 performed 250 iterations of adding random noise to a profile centered on the hilltop, and 250
233 iterations of random noise to a profile centered 0.5 m from the hilltop. These calculations
234 resulted in 500 values for the sediment transport coefficient that account for (1) sampling a
235 continuous hillslope with gridded data, (2) random noise from the DEM, and (3) a potential
236 mismatch between the actual location of the hillcrest and the highest pixel along the 1D ridge
237 in the DEM.
238

239 **3. Results**

240 We find that the 'raw' hilltop curvature (i.e., uncorrected for grid-scale effects) is
241 strongly correlated with the approximate square root of erosion rate: $C_{HT} \propto E^{0.48}$ (Figure 2).
242 The 'corrected' hilltop curvature is also correlated with erosion rate although the exponent in
243 the regression increases to 0.53 (Figure 3). In addition, the transport coefficient (calculated
244 from the corrected hilltop curvatures) varies with erosion rate, whereby $D \propto E^{0.47}$ (Figure 4).
245 The transport efficiency is not correlated with any of the climate parameters (Figure
246 5) nor with the 'effective energy and mass transfer' variable (plot not shown), a parameter
247 which incorporates both MAT and MAP to represent the influence of climate on soil
248 processes [*Rasmussen and Tabor*, 2007].

4. Discussion

Our results indicate that, at the sites we examined, erosion rate appears to have a dominant control on the efficiency of sediment transport. The apparent role of erosion rate on the efficiency of hillslope sediment transport and the insignificance of climate is unexpected considering that others have found a climatic influence on the value of D [*Hurst et al.*, 2013; *Richardson et al.*, 2019]. In contrast to our results, Richardson et al. [2019] compiled erosion rate and transport coefficient data from studies which used a variety of techniques to estimate these values, and their data included sites in a range of lithologies as well as from regions with a greater range in precipitation. As a result, their larger data set may be better suited for detecting an underlying climatic influence.

To explore how transport efficiency might increase with erosion rate, the factors contributing to soil creep can be assessed with two approaches. For discrete, intermittent large-scale soil creep events (e.g., tree throw), the transport efficiency can be calculated as

$$D = f_e \overline{V} \overline{d} \qquad (7)$$

where f_e is the frequency of events per unit area ($T^{-1}L^{-2}$), $\overline{V}$ is the average volume (L^3) of soil displaced with each event, and $\overline{d}$ is the average distance (L) that volume of soil is displaced [*Gabet*, 2000]. For example, in the case of tree throw, the transport coefficient will depend on the number of toppled trees over a period of time, the average volume of soil in the root plates, and the distance that the root plates are displaced [*Gabet et al.*, 2003]. We are not aware of any reason why any of these three factors would increase with erosion rate. Indeed, in the case of bioturbation, $\overline{V}$ and f_e might be expected to *decrease*. For example, because

soils tend to be thinner where erosion rates are high [e.g., *Gabet et al.*, 2015], the volume of soil available for transport by three throw should decrease. In addition, the frequency of bioturbation might be expected to decrease in rapidly eroding landscapes because of lower plant biomass [*Milodowski et al.*, 2014].

For dilational creep processes in which soil particles are lofted up and then settle down due to gravity, D can be expressed as [*Furbish et al.*, 2009]

$$D = kRh\overline{N_a\left(1-\frac{P}{P_m}\right)^2}\cos^2\theta \qquad (8)$$

where k is an empirically determined dimensionless constant that accounts for particle shape and the relationship between mean free path length and the vertical displacement of particles, R is particle radius (L), h is soil thickness (L), P is particle concentration (L^3L^{-3}), P_m is the maximum value of P, N_a is the particle activation rate (T^{-1}), θ is the hillslope angle (°) (equal to zero at the ridgecrest), and the overbar signifies vertically averaged quantities. The particle concentration (a function of soil bulk density) is not likely to be dependent on erosion rate to a significant degree and, if it is, the term in parentheses would likely decrease with increasing erosion rate, thereby suppressing the value of D. Because soils are thinner in rapidly eroding landscapes [e.g., *Gabet et al.*, 2015], variations in soil thickness also cannot account for the increase in transport efficiency with erosion rate; indeed, the inverse relationship between soil thickness and erosion rate should lead to an inverse relationship between D and E, the opposite of what we have found. With respect to particle activation rate, we are not aware of any studies that have correlated this variable with erosion rate; however, because rapidly

294 eroding hillslopes tend to have thinner and more exposed soils [e.g., *Gabet et al.*, 2015], the
295 particle activation rate in these landscapes could potentially be higher, which could lead to an
296 increase in D with E. For example, a decrease in vegetation biomass with increasing erosion
297 rate [*Milodowski et al.*, 2014] could leave the soil surface more vulnerable to raindrop impact
298 [*Dunne et al.*, 2010]. Nevertheless, as noted above, a reduction in biomass might also be
299 expected to damp bioturbation, thereby reducing the transport efficiency.
300 The final variable from Eqn. (8) to be explored is particle diameter, R. Previous
301 studies have documented an increase in particle diameter with erosion rate [*Attal et al.*, 2015;
302 *Riebe et al.*, 2015]. Where erosion is slow, particles are exposed to weathering processes for
303 longer periods of time because of longer soil residence times and, as a result, particles
304 become smaller [e.g., *Mudd and Yoo*, 2010]. In Eqn. (8), particle size is a factor in the
305 transport coefficient because it controls the mean free path of particles in a soil creeping by
306 dilational processes [*Furbish et al.*, 2009]. Although field data from Neeley et al. [2019]
307 suggest that coarser soils have a higher transport coefficient, laboratory experiments have
308 demonstrated that, for the same input of energy, coarse-grained soils will creep faster than
309 fine-grained soils [Supplement to *Deshpande et al.*, 2020]. In addition, of the various factors
310 that could affect the rate of soil creep, particle size is the one with the most potential to vary
311 by multiple orders-of-magnitude between watersheds eroding at different rates [*Marshall and*
312 *Sklar*, 2012]. For example, while the data are limited, particle radius along a ridgeline
313 increases with erosion rate at the Feather River site (Figure 6).
314 While particle size is a potential candidate for explaining the relationship between
315 transport efficiency and erosion rate found here, this hypothesis raises some perplexing
316 issues. First, whereas the relationship between particle size and erosion rate is likely to be

317 constant within a single region, one would expect them to vary between regions according to
318 climate and lithology (although we tried to control for rock strength, variations in texture, for
319 example, could affect particle size). However, despite the expected regional variations in
320 these factors, the sites fall along the same *D* vs. *E* trendline (Figure 3). Second, because the
321 more rapid weathering rates in wetter climates should lead to smaller soil particles [*Marshall*
322 *and Sklar*, 2012], the transport coefficient should decrease in wetter climates. However, we
323 find no relationship between mean annual precipitation and *D* (Figure 5).

324 Another potential explanation may be that the transport efficiency is sensitive to slope.
325 Landscapes that are eroding quickly are generally steeper than those that are eroding more
326 slowly. For example, the slopes at the ridgecrests (S_{HT}) at our sites increase with the
327 approximate square root of erosion rate (Figure 7). Some property of the soil (e.g., its
328 resistance to disturbance) may be affected by the gradient such that its transport efficiency
329 increases on steeper slopes (P. Richardson, pers. comm.). Furbish and Haff [2010] suggest
330 that the rate at which soil is mobilized might also increase with slope. To explore the
331 consequences of a slope-dependent transport coefficient, we define a new variable, D_s (L^2/T)

332 $$D_s = KS \tag{10}$$

333 such that

334 $$q_s = D_s S \tag{11a}$$

335 or

336 $$q_s = KS^2 \tag{11b}$$

337 where K (L^2/T) is a constant with the same properties as D. Inserting Eqn. (11b) into a
338 statement of mass conservation

339 $$\rho_r \frac{dz}{dt} = -\rho_s \frac{dq_s}{dx} \quad (12)$$

340 and integrating twice assuming steady state (dz/dt = E) and $\rho_r/\rho_s = 2$ yields

341 $$E = KCS/2 \quad (13a).$$

342 To specify that this relationship is applied to the hilltops, we rewrite it as

343 $$E = KC_{HT}S_{HT}/2 \quad (13b).$$

344 Thus, the assumption that the transport coefficient increases linearly with slope implies a
345 linear relationship between the erosion rate and the product of curvature and slope. Indeed, a
346 power-law regression between the two yields an exponent of unity, offering support for the
347 hypothesis that the transport coefficient is slope-dependent (Figure 8). However, because
348 slope and curvature are linearly related along a parabolic curve, Eqn. (13b) is functionally
349 equivalent to $E \propto C^2$ or $C \propto E^{1/2}$, which is the original relationship presented in Figure 3. In
350 other words, the linear relationship between E and $C_{HT}S_{HT}$ may simply be a mathematical
351 artefact, and the sediment flux relationship represented by Eqn. (11b) would need to be
352 validated independently. Finally, note that Eqn. (11b) is quite different from the nonlinear
353 sediment flux equation proposed elsewhere [*Andrews and Bucknam*, 1987; *Gabet*, 2003;
354 *Roering et al.*, 1999], particularly at lower slopes (Figure 9).

355 The lack of a clear and robust mechanistic link between D and E, as well as the square
356 root dependency of the hilltop curvature on erosion rate when Eqn. (2) predicts a linear
357 relationship, suggests that the present theory explaining the profile of soil-mantled hillslopes
358 is incomplete. We tentatively propose that, in resistant lithologies, hillslope curvature may be
359 partially, if not mostly, controlled by processes occuring within the bedrock, rather than the
360 soil. Indeed, in an eroding landscape, the soil on a hill is just a thin mantle covering a much
361 larger bedrock mass; the shape of the hill, therefore, should reflect the shape of the

underlying bedrock and the processes acting within it [e.g., *Rempe and Dietrich*, 2014]. However, the absence of any climatic influence in our results suggests that these bedrock processes are not associated with the typical chemical and physical weathering processes; instead, they are likely related to a more universal mechanism. Recent work has begun investigating how, even in soil-mantled landscapes, the generation of fractures in bedrock by topographic stresses may exert an important influence on landform shape [e.g., *Clair et al.*, 2015; *Pelletier*, 2017; *Slim et al.*, 2015]. However, whereas the regional tectonic stress is an important contributor to topographic stresses [e.g.,*Clair et al.*, 2015; *Miller and Dunne*, 1996], the tectonic stress regime varies widely between our sites. For example, the regional stresses are compressional in the San Gabriel Mountains but extensional in the Wasatch Mountains and the Feather River study area [*Heidbach et al.*, 2016; *Wakabayashi and Sawyer*, 2000]. Therefore, the alignment of these sites along the same trendline (Figure 2) suggests that our present understanding of rock fracture by topographic stresses is unable to explain our results.

One potential avenue for further investigations may be an examination of the time-dependent nature of fracture growth. At high erosion rates, near-surface bedrock is rejuvenated more quickly, thereby limiting the fracture density. In contrast, in environments where the erosion rate is slower and the rejuvenation of the surface occurs less frequently, the near-surface bedrock may have a higher fracture density as it accumulates damage over time. The relationship found here between hilltop curvature and erosion rate, therefore, may be related to the strength of the underlying rock mass in a way that is not yet understood. As a preliminary test of this idea, we analyzed the data from four sites that met our criteria but were underlain by presumably weak lithologies, sedimentary bedrock or highly sheared

metamorphic bedrock [*Perron et al.*, 2012; *Richardson et al.*, 2019]. A comparison of the hilltop curvatures between our original data-set consisting of resistant rocks and the data from the weaker lithologies suggests that, for the same erosion rate, the weaker bedrock forms hilltops with lower curvatures (Figure 10). While the data set from presumably weak lithologies is limited, it supports our hypothesis that weaker bedrock is associated with lower curvatures. Although one might argue that the lower curvatures seen in hillslopes underlain by weaker lithologies could be a result of higher transport efficiencies, a clear mechanistic link between bedrock strength and transport efficiency is lacking (see below), especially considering that most soil creep processes (e.g., tree throw) do not appear to be limited by soil texture.

If bedrock processes have an important influence on hillslope form, then hilltop curvature cannot be used for estimating the transport coefficient, at least in landscapes underlain by resistant rock. This limitation might explain why we were unable to detect any climatic influence on D, in contrast to compilations that include estimates of D from a variety of techniques [*Hurst et al.*, 2013; *Richardson et al.*, 2019]. In addition, if hillslope form is primarily dependent on the underlying bedrock, estimates of D based on topographic characteristics might be expected to be of different magnitudes than estimates from other techniques. Indeed, in the compilation presented by Richardson et al. [2019], transport coefficients estimated from relief and hilltop curvature are generally 5 – 10 times higher than those estimated from the modeling of scarps for the same aridity index (a factor that was determined to be a control on D) despite the fact that estimates based on scarp evolution were often performed on slopes comprised of unconsolidated sediment, which might be expected to have higher values of D. Therefore, the mismatch between the estimates of the transport

coefficient based on topographic metrics and those based on other techniques suggests that some other factor is influencing hillslope shape.

5. Conclusions

The square-root dependency of hilltop curvature on erosion rate challenges the prevailing theory linking soil creep to the shape of soil-mantled hillslopes, which predicts a linear relationship between the two. This dependency could be explained if the transport coefficient also varies with the square root of erosion rate. However, we are unable to propose a robust mechanism linking the transport coefficient to the erosion rate. Given the difficulties in accounting for our results within the standard theory of hillslope evolution, we tentatively propose that in landscapes underlain by resistant lithologies, hillslope curvature is not related to soil creep but is, instead, controlled by processes in the underlying bedrock.

Finally, the robust relationship between ridgetop curvature and erosion rate across a range of climatic conditions suggests that the latter can be estimated directly from topographic analysis in rock types similar to those analyzed in this study. However, erosion rates determined with this procedure must incorporate uncertainties in the original ^{10}Be erosion rate measurements, uncertainties in the curvature measurements, and the uncertainty in the regression between C_{HT} and E. Nevertheless, our results have the potential for providing a simple approach for estimating watershed-scale erosion rates through the measurement of hilltop curvatures.

Acknowledgments

Idaho field work for this project was conducted with assistance from B. Wood, S. Powell, and E. Hewitt. There were no real or perceived financial conflicts of interest for any

author nor did any author have an affiliation that could be perceived as having a conflict of interest with respect to the results of this paper. The data supporting the conclusions can be found in the tables and references. This project was partially funded by graduate student research grants from GSA and SJSU. LiDAR elevation data were acquired with a Seed Project from the National Center for Airborne Laser Mapping in the summer of 2011. Software used for analysis was developed under NERC grant NE/J009970/1. We are grateful to J. Pelletier, J. Roering, and P. Richardson for their careful reviews and helpful comments, and D. Furbish for extended and insightful discussions.

Data Availability Statement

Original data for this research are provided in Tables 1 and 2. Additional data were compiled from Belmont et al. [2007], Binnie et al. [2007], Dibiase et al. [2010], Duxbury [2009], Hurst et al. [2012], Richardson et al. [2019], and Riebe et al. [2001].

References

Anderson, H. W., G. B. Coleman, and P. J. Zinke (1959), Summer slides and winter scour, dry-wet erosion in Southern California mountains: U.S.D.A., Forest Service, *Pacific Southwest Forest and Range Experiment Station Technical Paper PSW-36*.

Anderson, R. S., S. P. Anderson, and G. E. Tucker (2013), Rock damage and regolith transport by frost: An example of climate modulation of the geomorphology of the critical zone, *Earth Surface Processes and Landforms, 38*(3), 299-316.

Andrews, D. J., and R. C. Bucknam (1987), Fitting degradation of shoreline scarps by a nonlinear diffusion model, *Journal of Geophysical Research, 92*(B12), 12,857-812,867.

Attal, M., S. M. Mudd, M. D. Hurst, B. Weinman, K. Yoo, and M. Naylor (2015), Impact of change in erosion rate and landscape steepness on hillslope and fluvial sediments grain size in the Feather River Basin (Sierra Nevada, California), *Earth Surface Dynamics, 2*, 1047-1092.

Belmont, P., F. J. Pazzaglia, and J. C. Gosse (2007), Cosmogenic 10Be as a tracer for hillslope and channel sediment dynamics in the Clearwater River, western Washington State, *Earth and Planetary Science Letters, 264*, 123-135.

Ben-Asher, M., I. Haviv, J. J. Roering, and O. Crouvi (2017), The influence of climate and microclimate (aspect) on soil creep efficiency: Cinder cone morphology and evolution along the eastern Mediterranean Golan Heights, *Earth Surface Processes and Landforms*, *42*(15), 2649-2662.

Binnie, S. A., W. M. Phillips, M. A. Summerfield, and K. Fifield (2007), Tectonic uplift, threshold hillslopes, and denudation rates in a developing mountain range, *Geology*, *35*, 743-746.

Binnie, S. A., T. J. Dunai, E. Voronina, T. Goral, S. Heinze, and A. Dewald (2015), Separation of Be and Al for AMS using single-step column chromatography, *Nuclear Instruments and Methods in Physics Research Section B: Beam Interactions with Materials and Atoms*, *361*, 397-401.

Brown, E. T., R. F. Stallard, M. C. Larsen, G. M. Raisbeck, and F. Yiou (1995), Denudation rates determined from the accumulation of in situ-produced 10Be in the Luquillo Experimental Forest, Puerto Rico, *Earth and Planetary Science Letters*, *129*(1-4), 193-202.

Carson, M. A., and M. J. Kirkby (1972), *Hillslope form and process*, 475 pp., Cambridge University Press, New York.

Clair, J. S., S. Moon, W. S. Holbrook, J. T. Perron, C. S. Riebe, S. J. Martel, B. Carr, C. Harman, K. Singha, and D. d. Richter (2015), Geophysical imaging reveals topographic stress control of bedrock weathering, *Science*, *350*, 534-538.

Culling, W. E. H. (1963), Soil creep and the development of hillside slopes, *Journal of Geology*, *71*, 127-161.

Denny, C., and J. Goodlett (1956), Microrelief resulting from fallen trees, *USGS Professional Publication*, *288*, 59-68.

Deshpande, N., D. J. Furbish, P. Arratia, and D. Jerolmack (2020), The perpetual fragility of creeping hillslopes, *EarthArXiv*, *doi:10.31223/osf.io/qc9jh*.

Dewald, A., et al. (2013), CologneAMS, a dedicated center for accelerator mass spectrometry in Germany, *Nuclear Instruments and Methods in Physics Research Section B: Beam Interactions with Materials and Atoms*, *294*, 18-23.

DiBiase, R. A., K. X. Whipple, A. M. Heimsath, and W. B. Ouimet (2010), Landscape form and millenial erosion rates in the San Gabriel Mountains, CA, *Earth and Planetary Science Letters*, *289*, 134-144.

Dunne, T., D. V. Malmon, and S. M. Mudd (2010), A rain splash transport equation assimilating field and laboratory measurements, *Journal of Geophysical Research - Earth Surface*, *115*(F01001), 1-16.

Duxbury, J. (2009), Erosion rates in and around the Shenandoah National Park, VA, determined using analysis of cosmogenic 10Be, MS thesis, 123 pp, University of Vermont.

Fernandes, N. F., and W. E. Dietrich (1997), Hillslope evolution by diffusive processes: the timescale for equilibrium adjustments, *Water Resources Research*, *33*(6), 1307-1318.

Furbish, D. J., and P. K. Haff (2010), From divots to swales: Hillslope sediment transport across divers length scales, *Journal of Geophysical Research*, *115*(F03001), doi:10.1029/2009JF001576.

Furbish, D. J., P. K. Haff, W. E. Dietrich, and A. M. Heimsath (2009), Statistical description of slope-dependent soil transport and the diffusion-like coefficient, *Journal of Geophysical Research*, *114*(F00A05), doi:10.1029/2009JF001267.

Gabet, E. J. (2000), Gopher bioturbation: Field evidence for nonlinear hillslope diffusion, *Earth Surface Processes and Landforms*, *25*(13), 1419-1428.

Gabet, E. J. (2003), Sediment transport by dry ravel, *Journal of Geophysical Research*, *108*(B1), 2050, 2010.1029/2001JB001686.

Gabet, E. J. (2020), Lithological and structural controls on river profiles and networks in the northern Sierra Nevada, *Geological Society of America Bulletin*, *132*(3-4), 655-667.

Gabet, E. J., O. J. Reichman, and E. Seabloom (2003), The effects of bioturbation on soil processes and sediment transport, *Annual Review of Earth and Planetary Sciences*, *31*, 259-273.

Gabet, E. J., S. M. Mudd, D. T. Milodowski, K. Yoo, M. D. Hurst, and A. Dosseto (2015), Local topography and erosion rate control regolith thickness along a ridgeline in the Sierra Nevada, California, *Earth Surface Processes and Landforms*, *40*(13), 1779-1790.

Gilbert, G. K. (1909), The convexity of hillslopes, *Journal of Geology*, *17*, 344-350.

Granger, D. E., J. W. Kirchner, and R. C. Finkel (1996), Spatially averaged long-term erosion rates measured from in situ-produced cosmogenic nuclides in alluvial sediment, *Journal of Geology*, *104*(3), 249-257.

Grieve, S. W. D., S. M. Mudd, and M. D. Hurst (2016), How long is a hillslope?, *Earth Surface Processes and Landforms*, *41*(8), 1039-1054.

Hack, J. T. (1973), Stream-profile analysis and stream-gradient index, *Journal of Research of the U.S. Geological Survey*, *1*(4), 421-429.

Hanks, T. C. (2000), The age of scarplike landforms from diffusion‐equation analysis, *Quaternary Geochronology: Methods and Applications*, 313-338.

Hanks, T. C., and D. P. Schwartz (1987), Morphologic dating of the pre-1983 fault scarp on the Lost River Fault at Doublespring Pass Road, Custer County, Idaho, *Bulletin of the Seismological Society of America*, *77*, 837-846.

Harel, M. A., S. M. Mudd, and M. Attal (2016), Global analysis of the stream power law parameters based on worldwide 10Be denudation rates, *Geomorphology*, *268*, 184-196.

Heidbach, O., M. Rajabi, K. Reiter, M. Ziegler, and W. Team (2016), World Stress Map Database Release 2016. V. 1.1, edited, GFZ Data Services.

Heimsath, A. M., D. J. Furbish, and W. E. Dietrich (2005), The illusion of diffusion: Field evidence for depth-dependent sediment transport, *Geology*, *33*(12), 949-952.

Hurst, M. D., S. M. Mudd, R. C. Walcott, M. Attal, and K. Yoo (2012), Using hilltop curvature to derive the spatial distribution of erosion rates, *Journal of Geophysical Research - Earth Surface*, *115*, 1-19.

Hurst, M. D., S. M. Mudd, K. Yoo, M. Attal, and R. C. Walcott (2013), Influence of lithology on hillslope morphology and response to tectonic forcing in the northern Sierra Nevada of California, *Journal of Geophysical Research - Earth Surface*, *118*, 832-851.

Kirchner, P. B., R. C. Bales, N. P. Molotoch, J. Flanagan, and Q. Guo (2014), LiDAR measurement of seasonal snow accumulation along an elevation gradient in the southern Sierra Nevada, California, *Hydrological Earth Systems Science*, *18*, 4261-4275.

Kohl, C. P., and K. Nishiizumi (1992), Chemical isolation of quartz for measurement of in-situ -produced cosmogenic nuclides, *Geochimica et Cosmochimica Acta*, *56*(9), 3583-3587.

Marshall, J. A., and L. S. Sklar (2012), Mining soil databases for landscape-scale patterns in the abundance and size distribution of hillslope rock fragments, *Earth Surface Processes and Landforms*, *37*(3), 287-300.

Mifsud, C., T. Fujioka, and D. Fink (2013), Extraction and purification of quartz in rock using hot phosphoric acid for in situ cosmogenic exposure dating, *Nuclear Instruments and Methods in Physics Research Section B: Beam Interactions with Materials and Atoms*, *294*, 203-207.

Miller, D. J., and T. Dunne (1996), Topographic perturbations of regional stresses and consequent bedrock fracturing, *Journal of Geophysical Research*, *101B*, 25,523-525,536.

Milodowski, D. T., S. M. Mudd, and E. T. Mitchard (2014), Erosion rates as a potential bottom-up control of forest structural characteristics in the Sierra Nevada Mountains, *Ecology*, *96*(1), 31-38.

Milodowski, D. T., S. M. Mudd, and E. T. A. Mitchard (2015), Topographic roughness as a signature of the emergence of bedrock in eroding landscapes, *Earth Surf. Dynam.*, *3*(4), 483-499.

Mudd, S. M. (2017), Detection of transience in eroding landscapes, *Earth Surface Processes and Landforms*, *42*(1), 24-41.

Mudd, S. M., and K. Yoo (2010), Reservoir theory for studying the geochemical evolution of soils, *Journal of Geophysical Research: Earth Surface*, *115*(F03030).

Mudd, S. M., M. Harel, M. D. Hurst, S. W. D. Grieve, and S. M. Marrero (2016), The CAIRN method: Automated, reproducible calculation of catchment-averaged denudation rates from cosmogenic radionuclide concentrations, *Earth Surface Dynamics*, *4*, 655-674.

Neely, A. B., R. A. DiBiase, L. B. Corbett, P. R. Bierman, and M. W. Caffee (2019), Bedrock fracture density controls on hillslope erodibility in steep, rocky landscapes with patchy soil cover, southern California, USA, *Earth and Planetary Science Letters*, *522*, 186-197.

Nishiizumi, K., M. Imamura, M. W. Caffee, J. R. Southon, R. C. Finkel, and J. McAninch (2007), Absolute calibration of 10be AMS standards, *Nuclear Instruments and Methods in Physics Research Section B: Beam Interactions with Materials and Atoms*, *258*(2), 403-413.

NOAA (2016), National Center for Environmental Information, edited.

Pelletier, J. D. (2017), Quantifying the controls on potential soil production rates: a case study of the San Gabriel Mountains, California, *Earth Surf. Dynam.*, *5*(3), 479-492.

Pelletier, J. D., et al. (2011), Calibration and testing of upland hillslope evolution models in a dated landscape: Banco Bonito, New Mexico, *Journal of Geophysical Research: Earth Surface*, *116*(F4).

Perron, J. T., P. W. Richardson, K. L. Ferrier, and M. Lapotre (2012), The root of branching river networks, *Nature*, *492*, 100-103.

PRISM (2014), PRISM Climate Group, edited.

595 Rasmussen, C., and N. Tabor (2007), Applying a quantitative pedogenic energy model across
596 a range of environmental gradients, *Soil Science Society of America Journal*, *71*(6),
597 1719-1729.
598 Rempe, D. M., and W. E. Dietrich (2014), A bottom-up control on fresh-bedrock topography
599 under landscapes, *Proceedings of the National Academy of Sciences*, *111*(18), 6576-
600 6581.
601 Richardson, P. W., J. T. Perron, and N. D. Schurr (2019), Influences of climate and life on
602 hillslope sediment transport, *Geology*, *47*, 423-426.
603 Riebe, C. S., J. W. Kirchner, D. E. Granger, and R. C. Finkel (2001), Minimal climatic
604 control on erosion rates in the Sierra Nevada, California, *Geology*, *29*(5), 447-450.
605 Riebe, C. S., L. S. Sklar, C. E. Lukens, and D. L. Shuster (2015), Climate and topography
606 control the size and flux of sediment produced on steep mountain slopes, *Proceedings*
607 *of the National Academy of Sciences*, *112*(51), 15574-15579.
608 Roering, J. J., J. W. Kirchner, and W. E. Dietrich (1999), Evidence for non-linear, diffusive
609 sediment transport on hillslopes and implications for landscape morphology, *Water*
610 *Resources Research*, *35*(3), 853-870.
611 Roering, J. J., J. W. Kirchner, and W. E. Dietrich (2001a), Hillslope evolution by nonlinear,
612 slope-dependent transport: steady state morphology and equilibrium adjustment
613 timescales, *Journal of Geophysical Research*, *106*(B8), 16499-16513.
614 Roering, J. J., J. T. Perron, and J. W. Kirchner (2007), Functional relationships between
615 denudation and hillslope form and relief, *Earth and Planetary Science Letters*,
616 *264*(1), 245-258.
617 Roering, J. J., J. W. Kirchner, L. S. Sklar, and W. E. Dietrich (2001b), Hillslope evolution by
618 nonlinear creep and landsliding: An experimental study, *Geology*, *29*(2), 143-146.
619 Roering, J. J., J. Marshall, A. M. Booth, M. Mort, and Q. Jin (2010), Evidence for biotic
620 controls on topography and soil production, *Earth and Planetary Science Letters*,
621 *298*, 183-190.
622 Saucedo, G. J., and D. L. Wagner (1992), Geologic map of the Chico quadrangle, California,
623 Division of Mines and Geology.
624 Slim, M., J. T. Perron, S. J. Martel, and K. Singha (2015), Topographic stress and rock
625 fracture: a two-dimensional numerical model for arbitrary topography and
626 preliminary comparison with borehole observations, *Earth Surface Processes and*
627 *Landforms*, *40*(4), 512-529.
628 Trabucco, A., and R. Zomer (2019), *Global Aridity Index and Potential Evapotranspiration*
629 *(ET0) Climate Database v2. CGIAR Consortium for Spatial Information*
630 *(CGIAR-CSI). Published online, available from the CGIAR-CSI GeoPortal at*
631 *https://cgiarcsi.community*.
632 Wakabayashi, J., and T. L. Sawyer (2000), Neotectonics of the Sierra Nevada and the Sierra
633 Nevada-Basin and Range transition, California, with field trip stop descriptions for
634 the northeastern Sierra Nevada, in *Field Guide to the Geology and Tectonics of the*
635 *Northern Sierra Nevada*, edited by E. R. Brooks and L. T. Dida, pp. 173 - 212,
636 California Division of Mines and Geology.
637 Wood, R. (2013), Transient hillslope response to an incision wave sweeping up a watershed:
638 a case study from the Salmon River, MS thesis, 42 pp, San Jose State University, San
639 Jose, CA.
640

641

642

643 Figure captions

644 **Figure 1.** Map of the United States showing the locations of the study sites.

645

646 **Figure 2.** Median hilltop curvature increases with the approximate square root of erosion
647 rate. Because ridgetops have negative curvature, the absolute value of curvature is plotted to
648 allow a power-law regression. For clarity, error bars are not shown here; uncertainties are
649 presented in Table 1.

650

651 **Figure 3.** Corrected median hilltop curvature vs. erosion rate. Accounting for grid-resolution
652 effects modifies the relationship between curvature and erosion rate, albeit only slightly
653 (compare with Figure 2).

654

655 **Figure 4.** Inferred transport efficiency (*D*) increases approximately with the square root of
656 erosion rate. *D* was calculated using the corrected hilltop curvatures.

657

658 **Figure 5.** Inferred transport efficiency (*D*) vs. various climatic measures. Inferred transport
659 efficiency does not depend significantly on mean annual precipitation (A), mean annual
660 temperature (B), or the aridity index (C). Note that the plot for mean annual temperature does
661 not include the data set from Richardson et al. [2019], which did not provide these values.

662

663 **Figure 6.** Geometric mean of particle size (*R*) increases with inferred erosion rate (*E*) at the
664 Feather River site [*Gabet et al.*, 2015]. Particle sizes of soil surface samples were measured
665 at regular intervals along a ridge with a gradient in erosion rates. Because local topography

along the ridgeline (i.e., saddles and knobs) was found to have a strong control on soil properties at this site, we present here only the data from the knobs. Erosion rate calculated from ridgetop curvatures using the relationship reported in the present study. 1σ for particle size data averages 5.8 mm (error bars not shown for clarity).

Figure 7. Mean slope at the ridgeline increases with erosion rate. The steeper slopes generally found in rapidly eroding landscapes can also be recognized along the ridgecrests.

Figure 8. Product of hilltop curvature and slope vs. erosion rate. The nearly linear relationship between the two supports a sediment flux law of the form $q_s = KS^2$. This linear relationship may be a mathematical artefact.

Figure 9. Comparison of nonlinear sediment flux equations. Dashed line represents the commonly used nonlinear equation calibrated with values determined in Roering et al. [1999]. Solid line represents fluxes calculated with Eqn. (11b) and calibrated to provide a comparison with the dashed line. Fluxes were calculated over the range of hilltop gradients measured at our field sites. Note that a linear regression (not shown) through the dashed line yields an R^2 of 0.9999, confirming the use of Eqn. (1) as an appropriate substitute for the standard nonlinear equation at low slopes.

Figure 10. Curvature vs. erosion rate according to rock type. For the same erosion rate, the hilltop curvature is lower at sites underlain with presumably weaker bedrock when compared to sites with stronger bedrock. Sites shown with the square markers are Tennessee Valley

689 (CA), Oregon Coast Range (OR), Gabilan Mesa (CA), and Allegheny Plateau (PA) [*Perron*

690 *et al.*, 2012; *Richardson et al.*, 2019].

691

Figure 1.

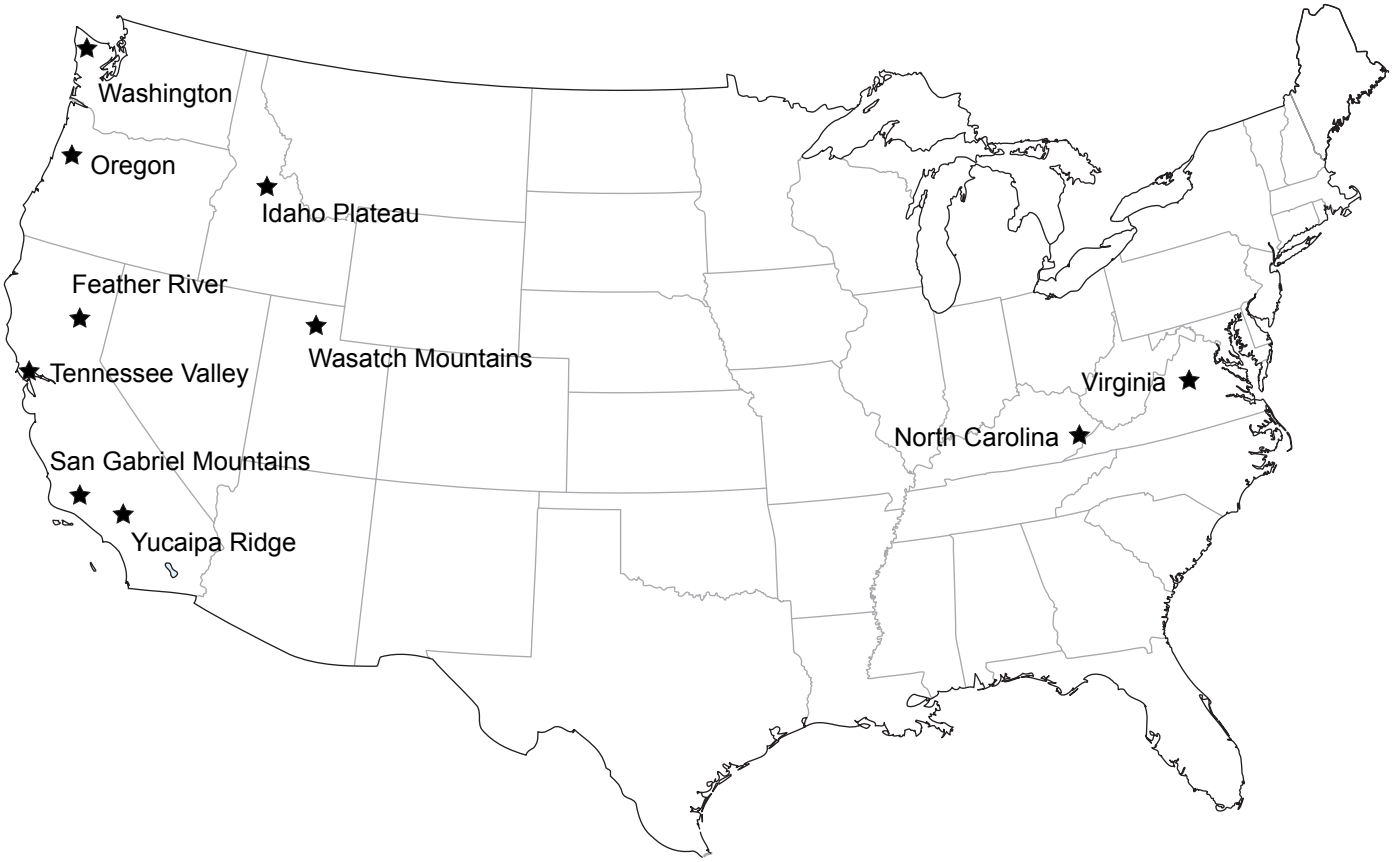

Figure 2.

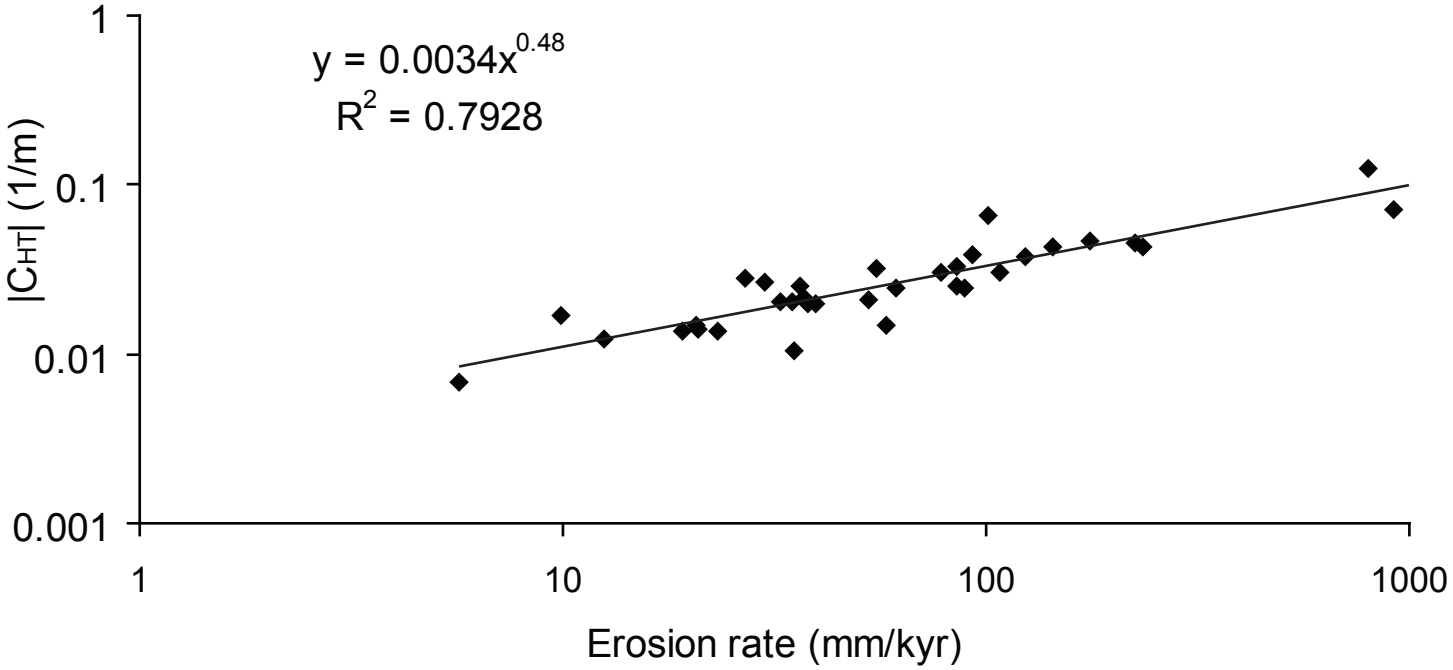

Figure 3.

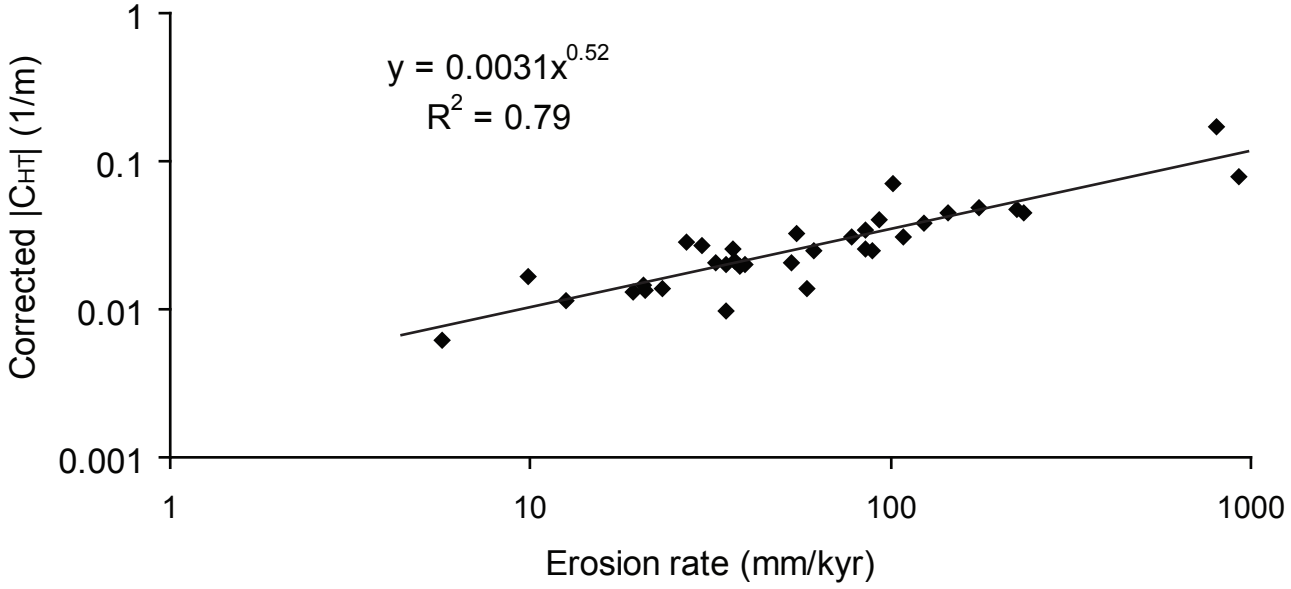

Figure 4.

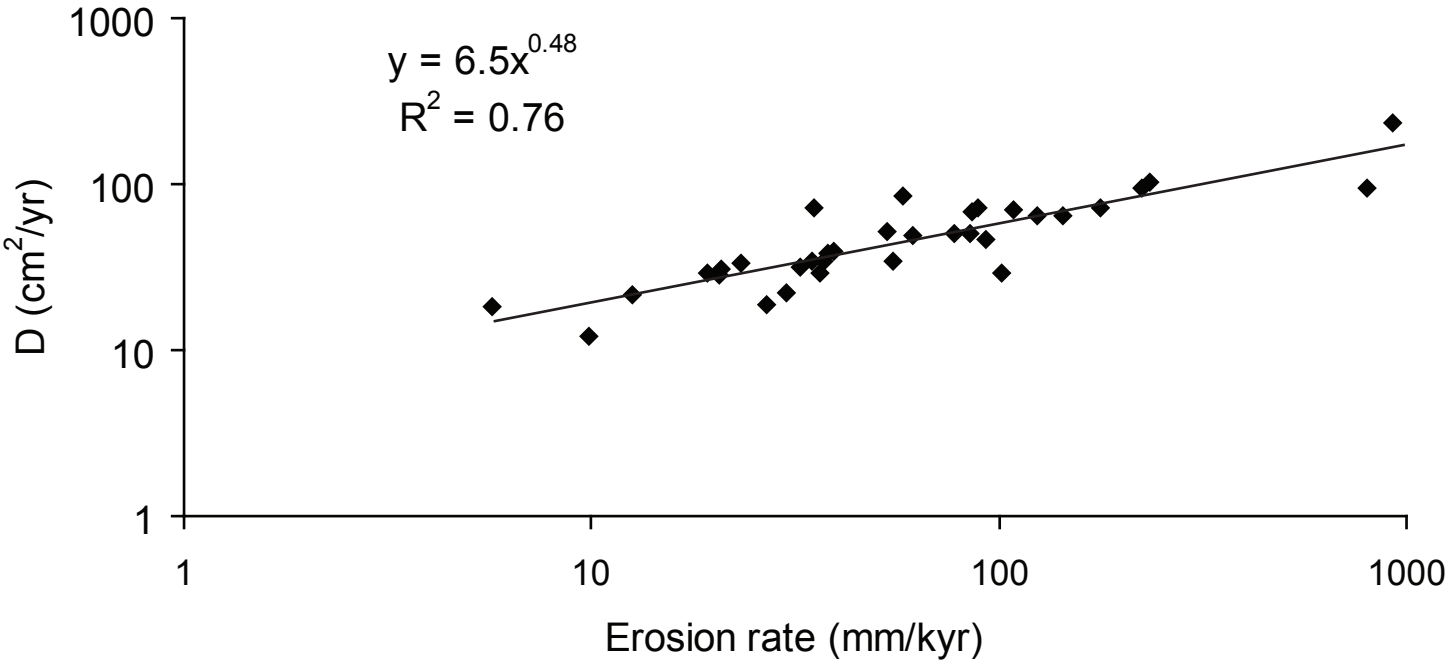

Figure 5.

(A)

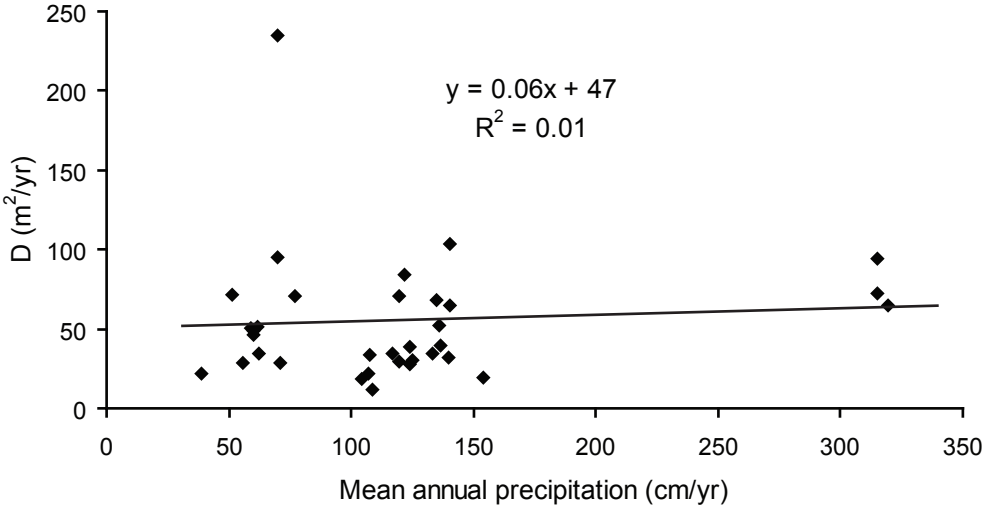

(B)

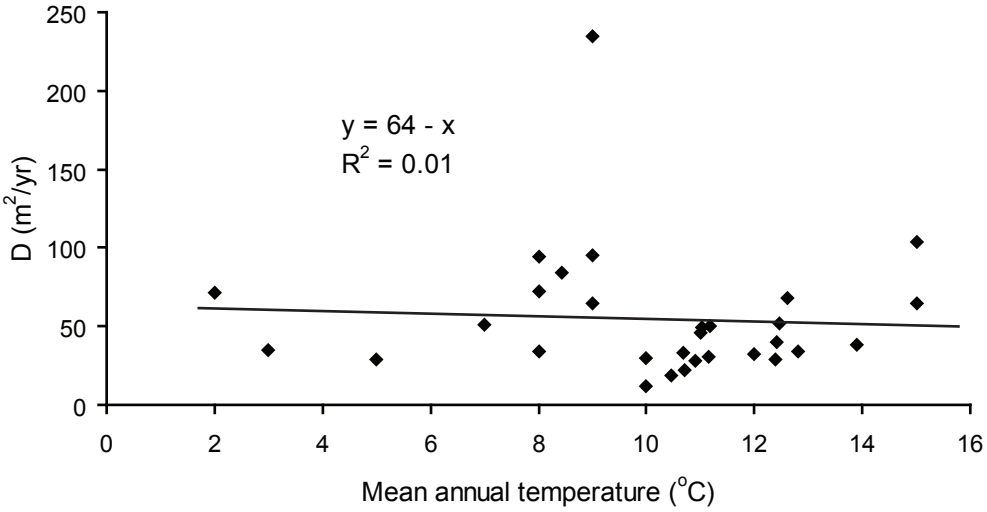

(C)

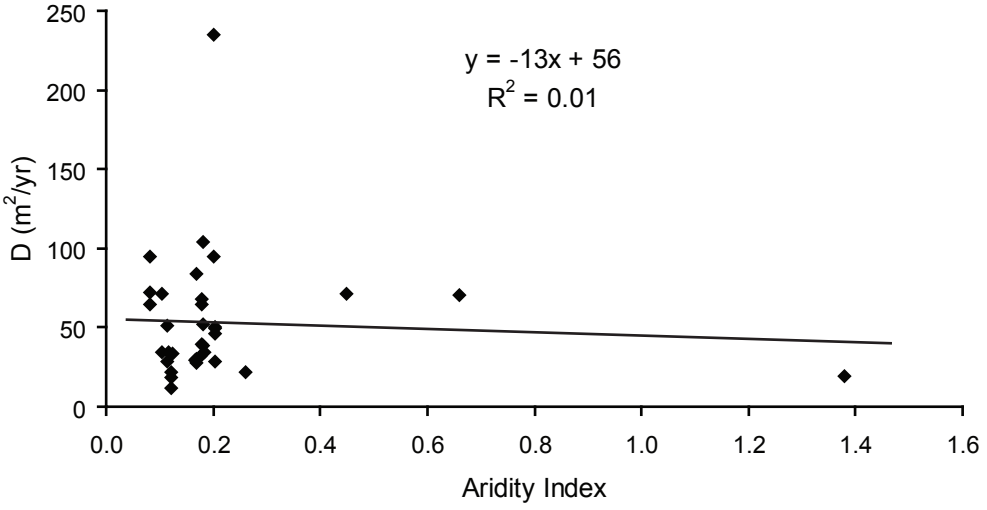

Figure 6.

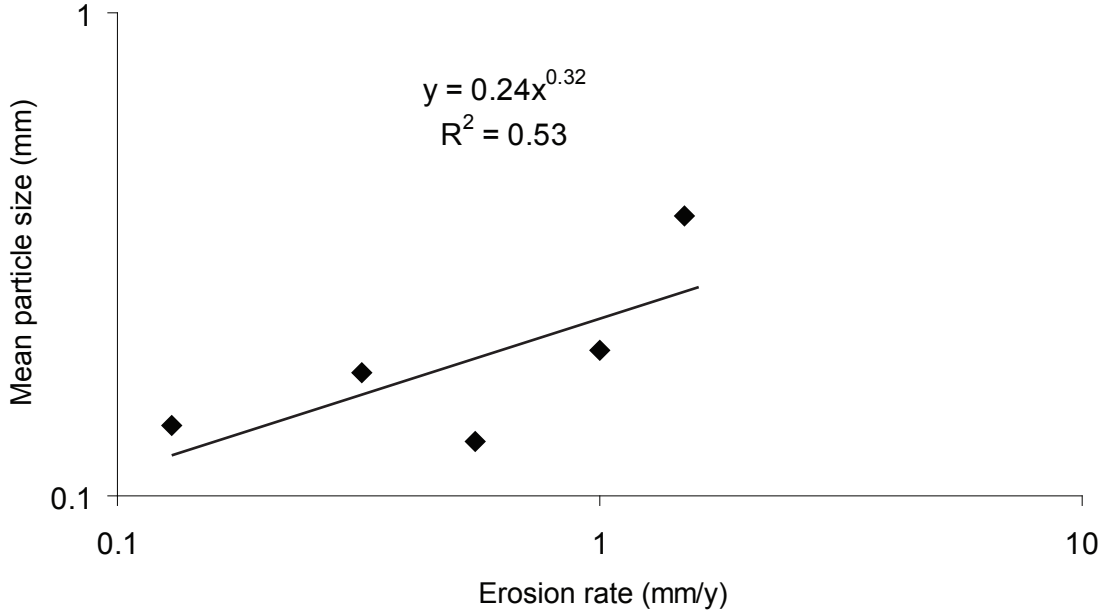

Figure 7.

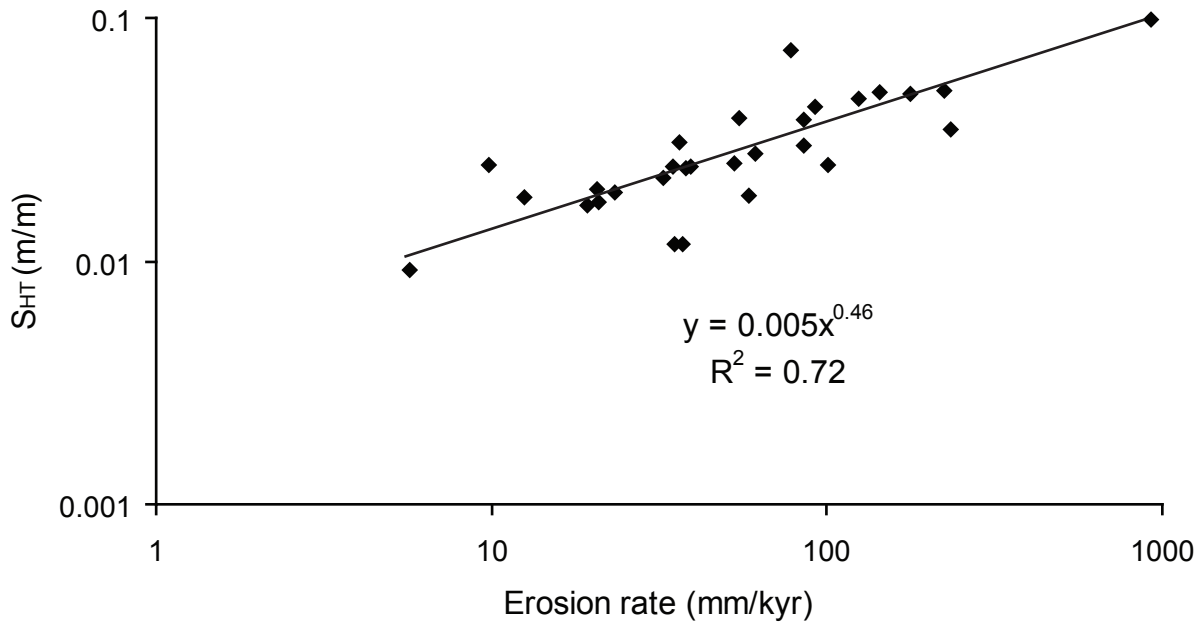

Figure 8.

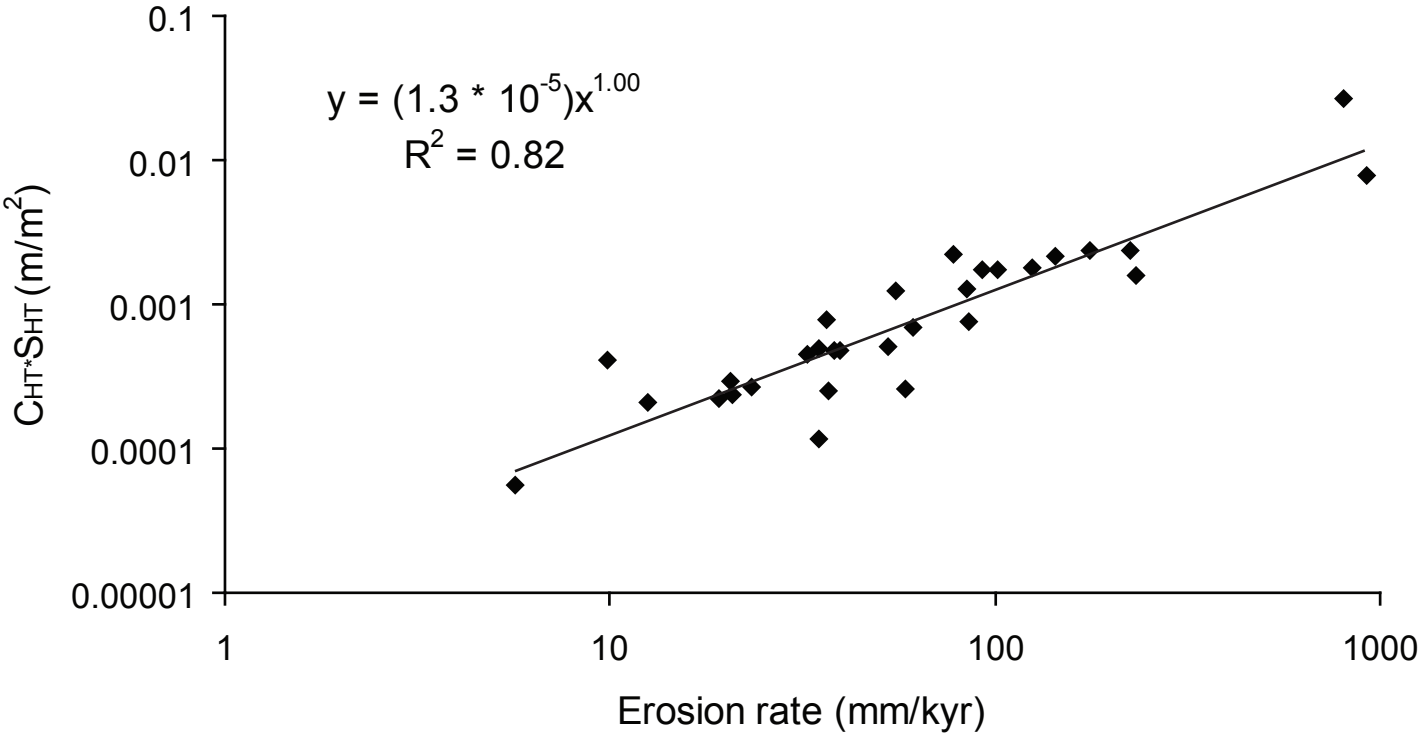

Figure 9.

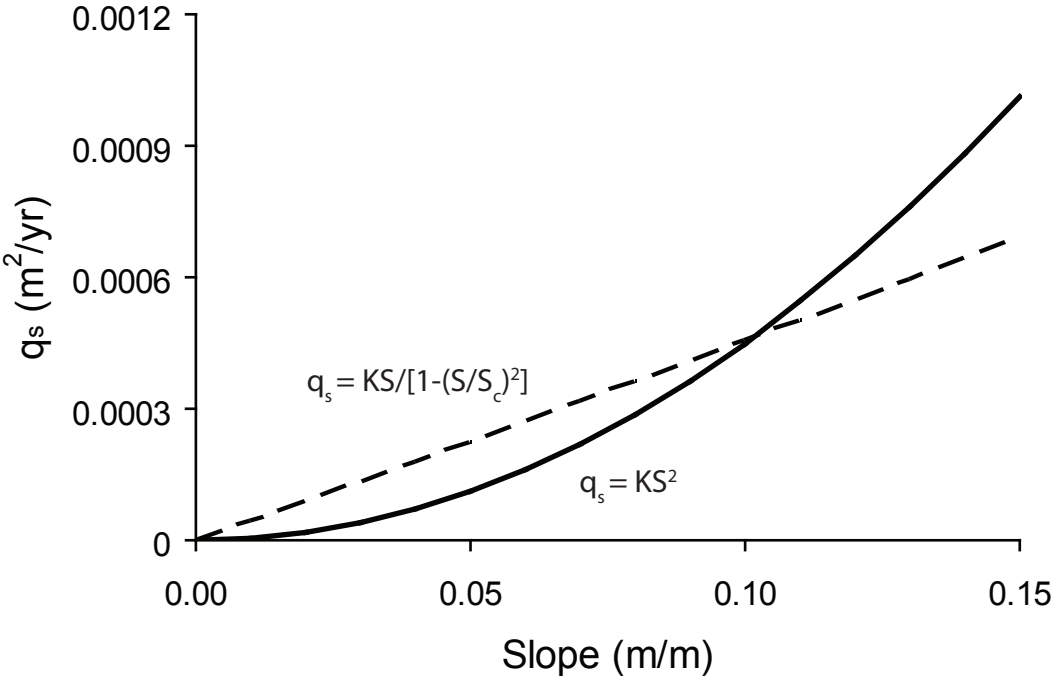

Figure 10.

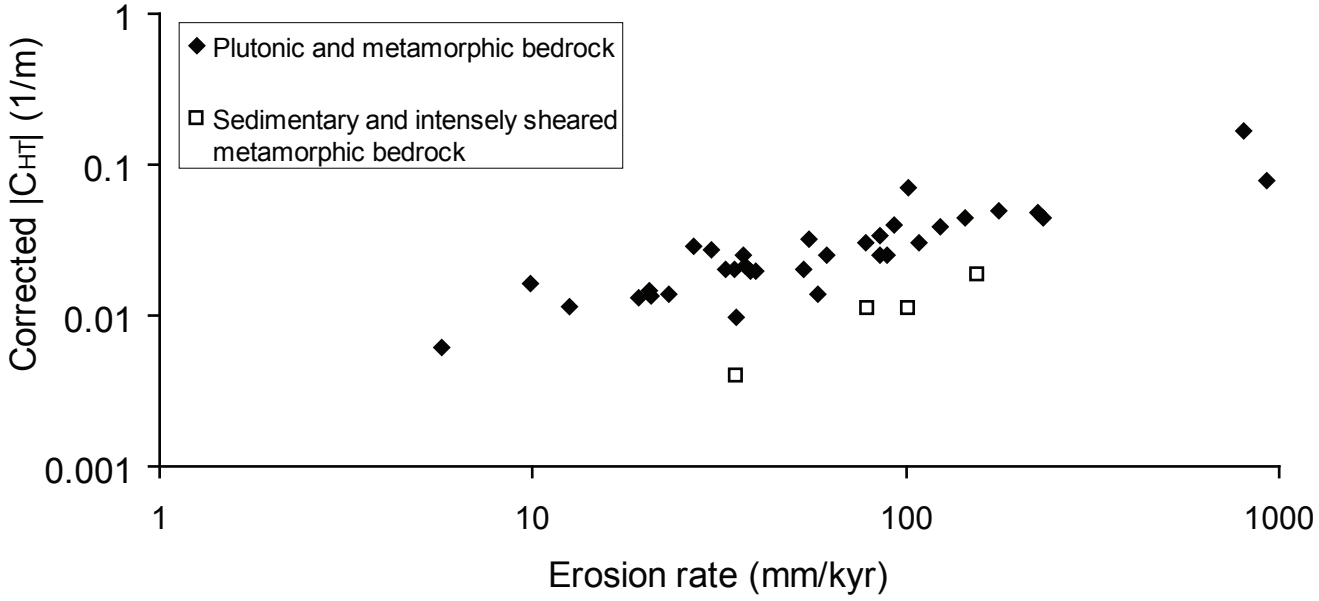

Table 1. Site information. (na = not available)

Region	Source	Sample ID	Latitude (°N)	Longitude (°W)	Lith-ology[j]	MAT[k] (°C)	MAP[k] (cm/yr)	Eros. ± 1σ (mm/kyr)	Med. Crv.[l] (1/m)	Ave. Slope (m/m)	D[l] ± 1σ (cm^2/yr)
San Gabriel Mountains (CA)	a	SG128	34.3376	118.0104	gr	12	55.5	37 ± 8	-0.02544	0.031	29 ± 6
	a	SG130	34.3783	117.9893	gr	11	59.8	62 ± 13	-0.02515	0.028	50 ± 10
	a	SG131	34.3666	117.9920	gr	11	58.8	85 ± 20	-0.03410	0.038	49 ± 12
	a	SG132	34.3658	117.9891	gr	11	60.1	93 ± 19	-0.04039	0.043	46 ± 9
	b	na	34.3640	117.9920	gr	na	77.1	108 ± 17	-0.03086	na	70 ± 12
Idaho Plateau (ID)	c	S1	45.4773	114.9618	tnlt	8	62.4	55 ± 11	-0.03254	0.039	34 ± 7
	c	S2	45.5008	114.9519	tnlt	5	71.0	101 ± 21	-0.07189	0.025	28 ± 7
	c	S3	45.5262	114.9293	tnlt	3	116.6	37 ± 7	-0.02139	0.012	34 ± 7
	c	R2	45.4843	114.9558	tnlt	7	61.8	78 ± 16	-0.03083	0.073	51 ± 11
	c	R3	45.5348	114.9015	tnlt	2	119.8	35 ± 7	-0.00971	0.019	72 ± 14
Yucaipa Ridge (CA)	d	3	34.0497	116.9280	qm, gns	9	70.1	922 ± 203	-0.08083	0.092	228 ± 57
	d	4	34.0530	116.9401	qm, gns	9	70.1	801 ± 175	-0.18688	0.159	86 ± 28
Blasingame (CA)	b	na	36.9540	119.6310	tnlt	na	38.7	30 ± 4	-0.02727	na	22 ± 3
Olympic Peninsula (WA)	e	U-WC-S	47.7399	124.0457	gw	8	315.1	177 ± 39	-0.04884	0.049	72 ± 17
	e	L-WC-S	47.7302	124.0379	gw	8	315.1	225 ± 51	-0.04755	0.050	95 ± 22
	e	L-EFMC-S	47.6581	124.2432	gw	9	319.6	144 ± 34	-0.04422	0.049	65 ± 16
Blue Ridge Mountains (VA)	f	SH-01a	38.5713	78.2873	gr	11	107.5	23 ± 5	-0.01391	0.019	33 ± 7
	f	SH-02a	38.6636	78.3550	mb	10	104.5	6 ± 1	-0.00616	0.009	19 ± 4
	f	SH-07	38.5816	78.4144	gr	10	108.6	10 ± 2	-0.01699	0.025	12 ± 2
	f	SH-10	38.6572	78.2822	gr	11	106.8	13 ± 3	-0.01203	0.018	21 ± 5
Feather River (CA)	g	BRB-2	39.6491	121.3020	qd	12	140.0	33 ± 7	-0.02036	0.022	32 ± 7
	h	BEAN-1	39.6126	121.3295	qd	13	133.2	35 ± 8	-0.02013	0.024	35 ± 7
	h	BEAN-2	39.6225	121.3283	qd	14	124.0	38 ± 8	-0.01969	0.024	39 ± 8
	h	BEAN-4	39.6237	121.3273	qd	12	136.1	53 ± 12	-0.02097	0.025	51 ± 11
	h	BEAN-5	39.6312	121.3298	qd	13	136.5	40 ± 8	-0.01954	0.024	40 ± 8
	i	BEAN-7	39.6284	121.3277	qd	13	134.7	85 ± 18	-0.02557	0.030	67 ± 14
	i	FT-3	39.6714	121.3109	qd	11	123.7	21 ± 4	-0.01425	0.017	29 ± 6
	i	FT-4	39.6712	121.3109	qd	11	124.8	21 ± 4	-0.01513	0.020	27 ± 6

	i	FT-6	39.6784	121.3155	qd	10	119.8	19 ± 4	-0.01338	0.017	29 ± 6
	i	SB-1	39.7189	121.2411	qd	8	121.9	58 ± 12	-0.01475	0.019	79 ± 17
	i	FR-4	39.6344	121.2771	qd	15	140.5	234 ± 79	-0.04535	0.035	103 ± 36
	i	FR-5	39.6354	121.2713	qd	15	140.5	124 ± 39	-0.03858	0.047	64 ± 21
Wasatch Mtns (Utah)	b	na	40.8920	111.8650	gr	na	51.5	89 ± 9	-0.02507	na	71 ±15
Great Smokey Mtns (NC)	b	na	35.6220	83.2040	qtz	na	154.0	27 ± 2	-0.02872	na	19 ± 1

[a] Source for ^{10}Be data and lithology: [*DiBiase et al.*, 2010]

[b] Source for all data: [*Richardson et al.*, 2019]

[c] Samples were collected for this study; source for lithology: [*Wood*, 2013]

[d] Source for ^{10}Be data and lithology: [*Binnie et al.*, 2007]

[e] Source for ^{10}Be data and lithology: [*Belmont et al.*, 2007]

[f] Source for ^{10}Be data and lithology: [*Duxbury*, 2009]

[g] Source for ^{10}Be data for all Feather River samples except FR-4 and FR-5: [*Hurst et al.*, 2012]

[h] Source for ^{10}Be data for FR-4 and FR-5: [*Riebe et al.*, 2001]

[i] Source for lithology: [*Saucedo and Wagner*, 1992]

[j] gr = granitic, tnlt = tonalite, qm = quartz monzonite, gns = gneiss, gw = greywacke, mb = metabasalt, qd = quartz diorite, qtz = quartzite

[k] applies to data from all sources except Richardson et al [2019]; MAT = mean annual temperature; MAP = mean annual precipitation; data from the PRISM Climate Group, http://prism.oregonstate.edu, accessed 25 March 2017

[l] Values corrected for grid-resolution effects. Grid-resolution adjustment for sites L-WC-S, L-EFMC-S, SH-01a, SH-02a used a 12-m analysis window because adustments using 14-window failed to converge to a solution. Sensitivity analyses indicate an average difference of <2% for curvature corrections using a window diameter of 12 m vs. 14 m.

Table 2. Details of ^{10}Be analysis from Idaho site.

Sample ID	Sample depth intervals (cm)	AMS measurement ID	^{10}Be concentration (x10^3 at g^{-1})	^{10}Be concentration uncertainty 1σ (x10^3 at g^{-1})
S1	0 - 2	s04446	119.9	5.7
S2	8 - 10	s04447	91.94	7.18
S3	16 - 18	s04448	373.7	17.8
R2	n/a	s04450	91.49	4.43
R3	n/a	s04451	408.8	15.1
R4	n/a	s04452	480.1	16.6